

ARTICLE OPEN



High frequency magnetometry with an ensemble of spin qubits in hexagonal boron nitride

Charlie J. Patrickson¹✉, Simon Baber¹, Blanka B. Gaál², Andrew J. Ramsay³ and Isaac J. Luxmoore¹

Sensors based on spin qubits in 2D crystals offer the prospect of nanoscale proximities between sensor and source, which could provide access to otherwise inaccessible signals. For AC magnetometry, the sensitivity and frequency range are typically limited by the noise spectrum, which determines the qubit coherence time. We address this using phase modulated continuous concatenated dynamic decoupling, which extends the coherence time towards the T_1 limit at room temperature and enables tuneable narrowband AC magnetometry. Using an ensemble of negatively charged boron vacancies in hexagonal boron nitride, we detect out-of-plane AC fields in the range of $\sim 10 - 150$ MHz, and in-plane fields within ± 150 MHz of the electron spin resonance. We measure an AC magnetic field sensitivity of $\sim 1 \mu\text{T}/\sqrt{\text{Hz}}$ at ~ 2.5 GHz, for a sensor volume of $\sim 0.1 \mu\text{m}^3$. This work establishes the viability of spin defects in 2D materials for high frequency magnetometry, with wide-ranging applications across science and technology.

npj Quantum Information (2024)10:5; <https://doi.org/10.1038/s41534-023-00796-4>

INTRODUCTION

Solid-state spin systems are a promising platform for the development of magnetic field sensors, with applications ranging from the the pursuit of quantum technologies to reaction monitoring in cells^{1–5}. Particular progress has been made with the nitrogen vacancy centre in diamond, thanks to long spin coherence times under ambient conditions. This has enabled significant progress, with notable highlights such as, single NV scanning magnetometers with nanoscale resolution^{6–10}, sub-millihertz resolution magnetic resonance spectroscopy^{11–13} and ensemble based devices with sensitivities in the $\text{pT}/\sqrt{\text{Hz}}$ range for signal frequencies ranging from DC¹⁴ and low frequency^{15,16} to GHz^{17,18}.

As the sensitivity depends on the spin coherence time, dynamical decoupling is often employed to shield the qubit from sources of noise, extending coherence times towards the T_1 limit. Pulsed variations using NV centres have achieved sensitivities in the $\text{nT}/\sqrt{\text{Hz}}$ range^{19,20}, however these are susceptible to errors arising from imperfect pulses^{3,21}. Continuous dynamical decoupling^{22–27}, on the other hand, avoids these issues and can also benefit from reduced power requirements³.

Recently explored spin defects in hexagonal Boron Nitride offer an interesting alternative. To date, the most well-studied spin system in hBN is the negatively charged boron vacancy²⁸ (V_B^-), which has been investigated as a sensor of temperature²⁹, strain^{30,31} and magnetic field^{29,32–35}. A potential limitation is the relatively short spin echo time^{36,37}. However, this can be mitigated with dynamic decoupling schemes^{35,36,38} and the 2D nature of the host material provides an opportunity for the sensor to be in close proximity to, or even embedded within, the system of interest^{32–34}.

In this work, we implement a continuous concatenated dynamic decoupling (CCDD) scheme²⁴ with an ensemble of boron vacancies, to simultaneously provide robust protection against dephasing, whilst also enabling high frequency magnetometry. This approach uses the CCDD drive field to manipulate spin state

transitions into resonance with a signal field. We characterise the sensor's performance at room temperature, demonstrating the detection of magnetic fields in the tens of MHz to several GHz range. For a fixed static magnetic field, the sensor has a bandwidth > 200 MHz and a sensitivity of $\sim 1 \mu\text{T}/\sqrt{\text{Hz}}$. We use the sensor to spatially map the magnetic field from a loop antenna and find good agreement between measurement, simulation and analytical solutions.

RESULTS

Theoretical background

The AC magnetic field sensor uses an ensemble of spin-1 negatively charged Boron vacancies in an hBN flake. The spin has a highly nonlinear response to an ac-magnetic field. This is used to mix the frequency of a signal field with the electron spin resonance, and an additional drive field. Optimising the drive field then produces a DC component of the signal field that can be detected as a change in fluorescence, known as optically detected magnetic resonance, thereby sensing the signal. The benefit of using this scheme for AC magnetometry is twofold. Firstly, the stabilising drive fields improve coherence times, increasing the sensitivity. Secondly, the resonant frequencies of the sensor can be tuned using a static magnetic field and the parameters of the drive field. As we shall see in the following sections, this results in a narrow sensor bandwidth, capable of determining the amplitude and frequency of an unknown signal in the MHz to GHz range.

Structure of the boron vacancy

The energy level diagram of the negatively charged boron vacancy is shown in Fig. 1a. Two unpaired electrons form a radiative spin triplet system (total spin quantum number, $S = 1$), with optical ground state zero-field splitting (ZFS) of $D_{GS} \approx +3.5$ GHz²⁸. The intersystem crossing rate, from triplet to singlet, is spin dependent ($\gamma_1 \approx 2\gamma_0$)³⁹, which enables initialisation

¹Department of Engineering, University of Exeter, Exeter EX4 4QF, UK. ²Department of Natural Sciences, University of Exeter, Exeter EX4 4QF, UK. ³Hitachi Cambridge Laboratory, Hitachi Europe Ltd., Cambridge CB3 0HE, UK. ✉email: cp728@exeter.ac.uk

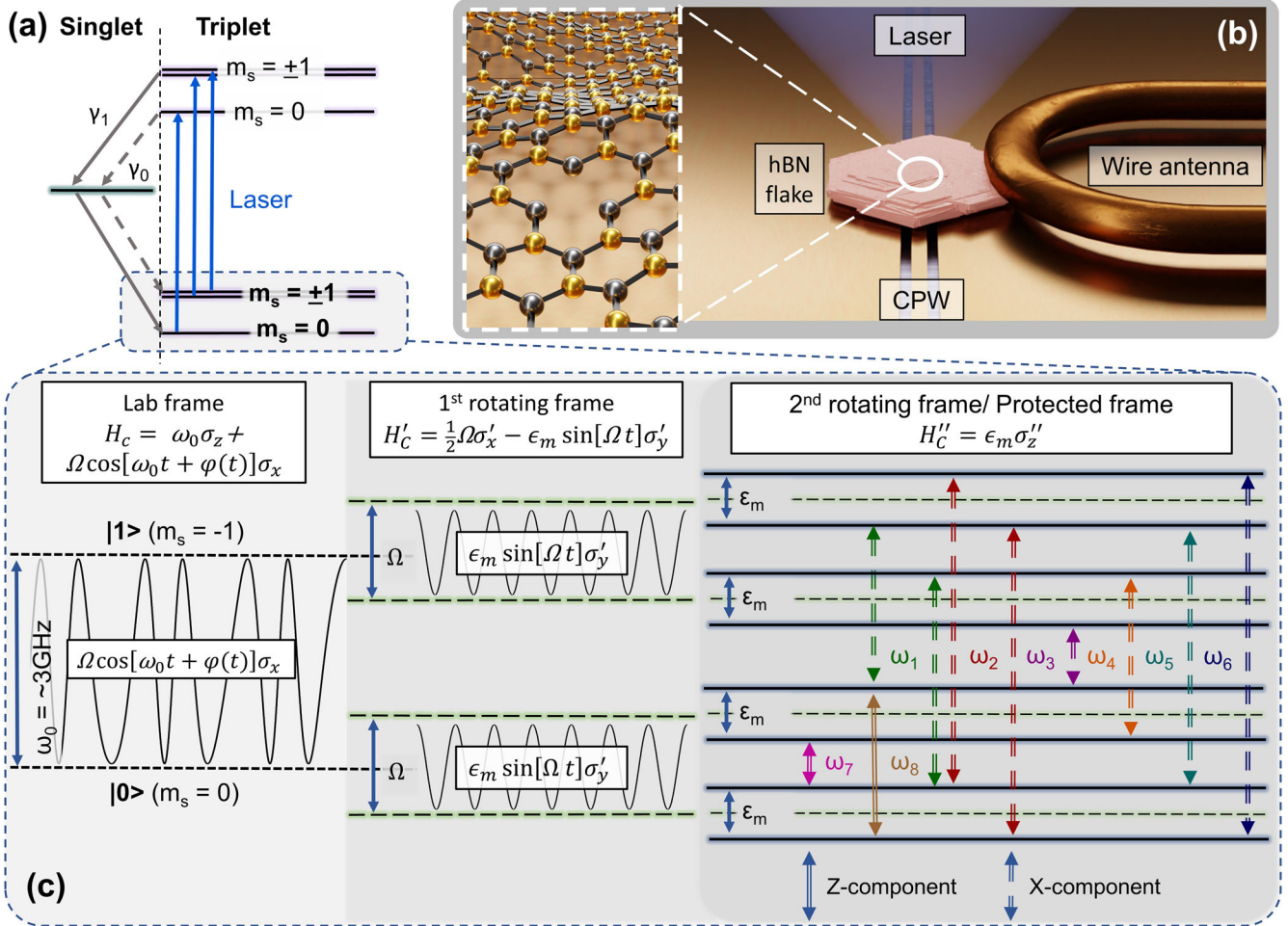


Fig. 1 Schematic of the system and sensing protocol used. **a** Simplified energy level diagram of the V_B^- defect in hexagonal boron nitride. **b** Illustration of the sensor and experimental setup with an inset depicting the boron vacancy. **c** Energy levels of the triplet ground state system under phase modulated concatenated dynamic decoupling. The concept of CCDD can be understood by viewing the system in frames of reference that rotate at the same frequency as the resonant MW drive fields; the first frame rotates at $\omega_0 \sigma_z$, the second rotates at $\Omega \sigma'_x$. Here we find static fields proportional to the amplitudes of the drive terms; Ω in the first frame, ϵ_m in the second. The sensing protocol relies on selection of the drive fields such that the signal field is resonant with one of the eight resonances $\omega_1 - \omega_8$, thereby driving that transition, resulting in a detectable change in spin state (see Eqs. (7) and (8)).

of the ground state spin in $m_s = 0$ via optical pumping, and spin readout via the photoluminescence (PL) intensity.

The electron Hamiltonian, H_e can be described by;

$$H_e = DS_z^2 + E(S_x^2 - S_y^2) + \gamma_e B_z S_z + H_C(t) + \delta H(t) \quad (1)$$

where $D = 3.45$ GHz and $E = 59$ MHz describe the ZFS terms in our sample³⁶, $\gamma_e \approx 28$ MHz/mT is the electron gyromagnetic ratio and S_i are the electron spin-1 operators. We apply a static magnetic field, B_z , parallel to the hBN c -axis. This separates the $|m_s = 0\rangle \leftrightarrow |m_s = \pm 1\rangle$ transitions. For a narrowband external ac magnetic field $H_C(t)$ near resonance with the energy gap ω_0 between the ground $|m_s = 0\rangle$ and $|m_s = -1\rangle$ states, the $|m_s = +1\rangle$ state can be neglected, reducing the system to a spin-half or qubit, with Hamiltonian $H_e \rightarrow \frac{\omega_0}{2} \sigma_z$. The final term, $\delta H(t)$ describes low frequency magnetic noise dominated by the electron-nuclear interaction. This limits the spin-echo times to under 100 ns^{36,37}, and therefore dictates the sensitivity to external magnetic fields.

Phase-modulated dynamic decoupling

In our previous work, we showed that decoherence arising from magnetic noise can be mitigated in V_B^- ensembles with CCDD³⁶.

Here, we choose phase, rather than amplitude, modulated CCDD. This has previously shown superior performance in extending the coherence time³⁶, which has a direct impact on sensor performance; the increase in contrast improves sensitivity by a factor of $e^{-t(\frac{1}{T_{amp}} - \frac{1}{T_{phase}})}$ ⁴⁰, where T_{amp} and T_{phase} are the coherence times associated with the two techniques. Additionally, this variation benefits from a reduction of $2\epsilon_m$ (see Eq. (2)) in the applied peak power. In both cases, the waveforms are created using an arbitrary waveform generator (AWG), and as such are similar in complexity.

The scheme is illustrated in Fig. 1(c), where a linearly polarised MW field of amplitude Ω is applied along the x axis to drive a Rabi oscillation between $|0\rangle$ and $|1\rangle$. A second drive is applied as an additional phase term, $\phi(t) = \frac{2\epsilon_m}{\Omega} \sin(\omega_m t - \theta_m)$. With this, we arrive at a MW control Hamiltonian of the form^{24,26,41}:

$$H_C = \frac{1}{2} \omega_0 \sigma_z + \Omega \cos(\omega t - \phi(t)) \sigma_x \quad (2)$$

Insight can be gained by viewing the system in a frame of reference rotating at the drive frequency ω . Here, we find $H'_C = e^{i\omega t \sigma_z / 2} H_C e^{-i\omega t \sigma_z / 2} - \omega \sigma'_z / 2$

$$H'_C = \frac{1}{2} (\omega_0 - \omega) \sigma'_z + \frac{1}{2} \Omega \sigma'_x + \frac{1}{2} \Omega \phi(t) \sigma'_y \quad (3)$$

where $'$ refers to axes in the first rotating frame, we have applied the RWA and take the limit $\epsilon_m \ll \Omega$. In the case of a single drive ($\epsilon_m = 0$), resonant with the electron spin resonance ($\omega = \omega_0$), we find a static energy gap of $\Omega\sigma'_x$ - the eigenvalues of the first dressed state. By selecting $\omega_m = \Omega$, in the case of a double drive ($\epsilon_m \neq 0$) the phase modulation term, $\phi(t)$, drives transitions between the first dressed states, shown in the middle panel of Fig. 1(c).

Moving to a second frame of reference rotating around the x' -axis at the $\phi(t)$ frequency ω_m , we find

$$H''_c = \frac{1}{2}(\Omega - \omega_m)\sigma'_x + \frac{1}{2}\epsilon_m(\sigma'_y \sin(\theta_m) + \sigma'_z \cos(\theta_m)) \quad (4)$$

where we have again applied the RWA and taken the limit $\epsilon_m \ll \Omega$. We refer to this second rotating frame of reference, shown in the right hand panel of Fig. 1(c), as the *protected frame*. This space is robust against the dominant sources of noise, as demonstrated in the following section. Setting $\omega_m = \Omega$ results in a static energy gap of amplitude ϵ_m in the protected frame, with an axis that can be selected using the phase of the second drive term, θ_m . Here, an ideal Rabi oscillation is represented by the spin-vector $\sigma'' = (0, 0, -1)$.

Overall, this frame describes a pair of spin states, separated by an energy gap of ϵ_m that rotate around both the z and x' axes, at frequencies ω , and ω_m . This results in states that are dynamically decoupled from both bit and phase-flip errors, extending the coherence times towards the T_1 limit.

AC magnetometry

In the lab frame, an AC signal of frequency ω_s is described by an additional drive term, H_{AC} , in the Hamiltonian.

$$H_{AC\perp} = g_{\perp}\sigma_x \cos(\omega_s t + \phi_s) \quad (5)$$

$$H_{AC\parallel} = g_{\parallel}\sigma_z \cos(\omega_s t + \phi_s) \quad (6)$$

where $g_{\parallel} = \frac{1}{2}\gamma_e B_{\parallel}$ and $g_{\perp} = \frac{1}{2}\gamma_e B_{\perp}$. Transforming to the protected frame, the signal term becomes (see Supplementary Note 2):

$$H''_{AC\perp} = \frac{1}{4}g_{\perp} \left[\sigma'_z \cos((\omega_s - \omega)t + \phi_s) - \sum_{\nu=+,-} S_{\nu} e^{i\nu((\omega_s - \omega - \nu\omega_m)t + \phi_s)} + h.c. \right], \quad (7)$$

$$H''_{AC\parallel} = \frac{1}{2}g_{\parallel} \left[\sum_{\nu=+,-} S_{\nu} e^{-i((\omega_s - \nu\omega_m)t + \phi_s)} + h.c. \right]. \quad (8)$$

where we have applied an additional rotation around the y'' axis to arrive at a more concise form. In the protected frame, the signal term can drive a Rabi oscillation when one of the shifted frequencies is resonant with the ϵ_m splitting of the protected spin, and can be detected via spin dependent PL. Eight signal frequencies meet this condition: $\omega_s = \omega_0 \pm \epsilon_m$ and $\omega_s = \omega_0 \pm \epsilon_m \pm \omega_m$ for in-plane signals, and $\omega_s = \omega_m \pm \epsilon_m$ for out of plane signals (see ω_1 to ω_8 in Fig. 1c). The signal frequency can be determined by tuning the resonances via the CCDD drive parameters. Moreover, because the resonance conditions hold for any value of the signal phase ϕ_s , phase locking between the signal and microwave control waveform is not necessary.

The magnetic noise can be described as $\delta H(t) = \sum_{\omega_{\beta}, \alpha} \sigma_{\alpha} B_{N,\alpha}(\omega_{\beta}) \cos(\omega_{\beta} t)$. This takes the same form as H_{AC} and transforms to the protected frame in the same way. By optimising the CCDD scheme, the noise spectrum can be frequency shifted away from resonance with the qubit, reducing decoherence. The primary source of noise is low frequency electron-nuclear interactions along the z -axis. In the protected frame, decoupling from nuclear noise requires $\omega_{\beta} \pm \omega_m \neq \epsilon_m$, which holds for low frequencies of ω_{β} associated with electron-

nuclear coupling. The second largest source of noise comes from slow fluctuations in drive amplitude, Ω , where the requirements are $\omega_{\beta} - \omega_0 \pm \omega_m, \omega_{\beta} + \omega_0 \pm \omega_m, \omega_{\beta} \pm \omega_0 \neq \epsilon_m$.

Sample and experimental setup

In our experiments we use an ensemble of Boron vacancies in an hBN flake, transferred to a co-planar waveguide on a sapphire substrate^{36,39} (see Fig. 1a). The MW control fields are applied to the CPW using an AWG. To demonstrate that the scheme does not require phase locking between signal and control fields, we use a separate signal generator to drive the signal, which we apply to either the CPW or, in later experiments, to a 40 μm diameter wire mounted on an XYZ translation stage (Fig. 1b). All measurements are made at room temperature. PL (>750 nm) is excited using a 488 nm laser and detected with a single photon avalanche diode (see "Methods" for further experimental details).

AC field sensing protocol

The pulse sequence used for AC-field sensing is illustrated in Fig. 2a and consists of two repeating sequences of qubit initialisation, spin manipulation, and readout. The first laser pulse initialises the ensemble into the $|0\rangle$ state. Next, the spin is manipulated with a MW control sequence, before a second laser pulse excites PL, which is recorded as P_0 . This laser pulse also reinitialises the spin for the second MW manipulation, which is again followed by a measurement of the PL, P_+ . In the two sequences, the waveform $\omega_{MW} = \Omega \cos[\omega_0 t - \frac{2\epsilon_m}{\Omega} \sin(\omega_m t)]$ is applied with $\Omega = \omega_m = (2\pi)$ 100 MHz, but for total times, $T = T_{MW}$ and $T = T_{MW} + \Delta T$, respectively. We use the contrast, $C = (P_0 - P_+)/P_+$, as the sensor readout parameter. A typical measurement of the contrast is plotted in blue in Fig. 2b, where $\Delta T = 1/(2\Omega) = 5$ ns is fixed and T_{MW} is swept, effectively measuring the derivative of the CCDD stabilised Rabi-oscillation. This has the advantage of cancelling the effect of T_1 relaxation³⁶ and maximizes the contrast, and therefore sensitivity to an external signal.

In the presence of an in-plane continuous external signal applied via the CPW with $\omega_s = \omega_0 + \epsilon_m = (2\pi)2.557$ GHz the sensor undergoes two Rabi cycles at two different Rabi frequencies, simultaneously. The first is the CCDD stabilised lab frame Rabi oscillation with frequency Ω . The second is driven by the signal field in the protected frame, with a Rabi frequency proportional to the signal amplitude g_{\perp} . The difference in Rabi frequencies produces a beating effect, as shown in orange in Fig. 2b. In the Fourier domain, this manifests as a Mollow triplet centred on the lab frame Rabi frequency Ω , with two sidebands offset by the Rabi frequency of the signal in the protected frame, $g_{\perp}/2$ (Fig. 2d). This provides a method to determine the signal amplitude, which is used to calibrate the sensor (see Supplementary Note section 1).

Sensor performance

To evaluate the sensing protocol, in Fig. 3 we quantify the sensor performance in response to an in plane signal, g_{\perp} , delivered through the CPW. Whilst the signal-driven Rabi-oscillation measurement in Fig. 2b can determine the signal amplitude and provides a means to calibrate the sensor, it is inconvenient to make such a measurement repeatedly, for example when determining the frequency or spatial extent of a signal. Instead, we employ a type of variance detection⁴², where we specifically select $T_{MW} = N/\Omega$, where N is an integer, and $\Delta T = 1/2\Omega$ in order to compare adjacent peaks and troughs of the lab frame Rabi oscillation, thereby maximising the readout contrast, and hence the sensitivity.

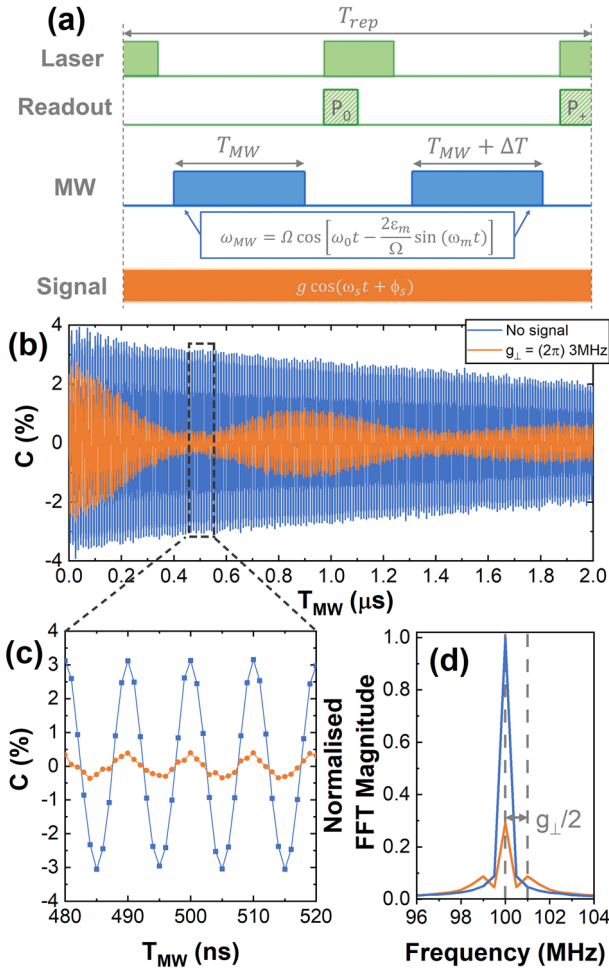


Fig. 2 AC Field Sensing Protocol using signal driven Rabi-oscillations of the CCDD protected qubit. **a** Optimised pulse-sequence for AC field sensing. Alternating microwave pulses of length T_{MW} and $T_{MW} + \Delta T$ are interlaced with laser pulses for preparation and readout of the spin. We define contrast as $(P_0 - P_+)/P_+$; P_0 (P_+) is the measured PL following a microwave pulse of length T_{MW} ($T_{MW} + \Delta T$). For AC sensing we choose $\Delta T = 1/(2\Omega)$. **b** Measurement using the pulse sequence described in **(a)**, highlighting the CCDD stabilised Rabi-oscillation ($\Omega = (2\pi)100$ MHz and $\epsilon_m = (2\pi)30$ MHz). Shown with and without signal, $H_{AC\perp}$ with $\omega_s = (2\pi)2.577$ GHz. **c** Close up of **(b)** around $T_{MW} = 500$ ns. **d** Fourier transforms of **(b)**. The signal driven Rabi oscillation in the protected frame manifests as the sidebands of a Mollow triplet.

We begin by measuring the contrast as a function of signal frequency, with fixed CCDD parameters $\Omega = \omega_m = (2\pi)100$ MHz, $\epsilon_m = (2\pi)30$ MHz, $T_{MW} = 300$ ns and $\Delta T = 5$ ns (Fig. 3a). Sweeping the signal frequency in a 300 MHz range around the electron spin resonance at ω_0 , the sensor detects six resonances, as predicted in Eq. (7). Using a Lorentzian fit the average linewidth is 3.9 MHz, which determines the frequency resolution of the sensor. In Fig. 3b we show how an unknown signal frequency can be determined. Whilst recording the contrast, the CCDD drive is used to tune the sensor into resonance with the signal by sweeping ϵ_m . The six resonances shift as expected, and we achieve a detectable frequency range ± 150 MHz with respect to ω_0 . In principle, a similar measurement can be made by sweeping Ω and the frequency range can also be extended by changing the static magnetic field that determines ω_0 . The lower frequency limit on a detectable signal is expected to be around 200 MHz, due to

increased decoherence close to the ground state level anti-crossing^{39,43,44}. The upper limit is bound by the frequency limit of the microwave electronics and the strength of the static magnetic field. However, it is realistic to expect that the sensor could operate in a similar manner for signals up to tens of GHz.

Next, with the signal tuned to the $\omega_s = \omega_0 + \epsilon_m \approx (2\pi)2.557$ GHz resonance, we quantify the amplitude sensitivity to an in-plane AC B-field. In Fig. 3(c) the change in contrast, $\Delta C = |C_0 - C_s|$, where C_s (C_0) is contrast with (without) the signal applied, is plotted as a function of the signal amplitude, for three different T_{MW} (see Supplementary Note section 1 for signal calibration). The sensor is most sensitive, where the gradient, $\frac{\partial(\Delta C)}{\partial B}$ is maximum, which is shown for $T_{MW} = 300$ ns as the green dashed line in Fig. 3c. From this, we calculate the minimum resolvable change in magnetic field⁴⁰,

$$\delta B_{min}(t_m) = \frac{\sigma(t_m)}{\max\left|\frac{\partial(\Delta C)}{\partial B}\right|} \quad (9)$$

where $\sigma(t_m)$ is the standard deviation of ΔC as a function of the measurement time t_m . To measure $\sigma(t_m)$, ΔC is repeatedly sampled at 1 ms time intervals and the resulting values of $\delta B_{min,\perp}(t_m)$ are plotted in Fig. 3d. $\delta B_{min,\perp}$ follows the expected square root dependence for Shot noise limited detection, up to total measurement times of tens of seconds, when drifting laser power becomes significant. For $t_m < 10$ s, the sensitivity, $\eta_{\perp} = \delta B_{min,\perp}(t_m)\sqrt{t_m}$ is $\sim 1 \mu\text{T}/\sqrt{\text{Hz}}$, which is currently limited by the data rate of our time-tagging electronics (see “Methods”).

The measured sensitivity is similar to reported figures for DC and MHz magnetic field sensing using ensembles of boron vacancies, where values of $\sim 2 \mu\text{T}/\sqrt{\text{Hz}}$ have been achieved^{35,45}, but considerably larger than state-of-the-art NV-centre based GHz frequency sensors, where sensitivities can reach the pT/ $\sqrt{\text{Hz}}$ range^{17,18}. This difference in performance is largely due to a difference in sensor volume, V , with the diamond devices having volumes of $V \sim 0.04 \text{ mm}^3$ ¹⁷ and 0.63 mm^3 ¹⁸, compared to $\sim 0.1 \mu\text{m}^3$ in our case. Some applications preclude the use of large sensing volumes, for example when measuring signals from individual or small numbers of spins⁴⁶, in which case scaling the sensitivity by the volume provides a more representative metric of performance. Assuming a uniform defect density, the scaled sensitivity, $\tilde{\eta} = \eta\sqrt{V}$, gives figures of $\tilde{\eta} \sim 2 \text{ pTHz}^{-1/2} \text{ mm}^{3/2}$ for the diamond sensors compared to $\tilde{\eta} \sim 10 \text{ pTHz}^{-1/2} \text{ mm}^{3/2}$ in this case. For signals that originate from larger sources, this also suggests that significant gains in sensitivity could be made by increasing the sensor volume (and/or defect density), assuming the laser power density is maintained. There is also an inherent trade-off between spatial resolution and the sensor volume, with the requirements driven by the particular application.

Figure 3(c) also illustrates how T_{MW} can be selected according to the required dynamic range. For small amplitude signals the sensitivity is improved with a longer T_{MW} , whereas for larger signal amplitudes, the monotonic range of the sensor can be increased by selecting a shorter T_{MW} . This is a direct consequence of the fact that we are measuring a signal driven Rabi oscillation; the larger the signal field, the faster the protected frame Rabi oscillation and the earlier we can detect a change in contrast, thereby affording a shorter T_{MW} .

External AC magnetic field

Thus far, the experiments have been focused on signals applied from an independent source via the CPW, which is designed to achieve a large in-plane magnetic field. This simulates the case of a signal collected by an antenna and directed to the sensor. To simulate the direct detection of a signal, we instead use a nearby loop of 40 μm diameter wire mounted on an XYZ translation stage (Fig. 1b), driven by an independent signal generator. This is first

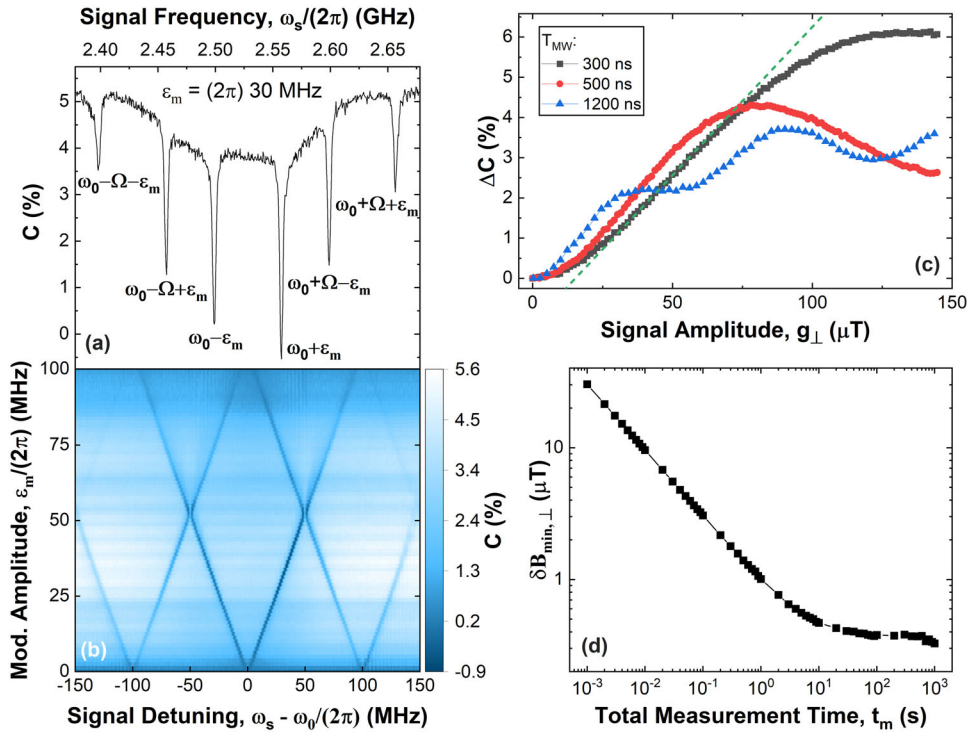


Fig. 3 Sensor response to in-plane AC magnetic fields, g_{\perp} . **a** Sensor frequency response for Rabi Frequency, $\Omega = (2\pi)100$ MHz and modulation amplitude, $\epsilon_m = (2\pi)30$ MHz, showing narrow bandwidth response at frequencies $\omega_s = \omega_0 \pm \epsilon_m$ and $\omega_s = \omega_0 \pm \Omega \pm \epsilon_m$. **b** Tuning of sensor frequency response with ϵ_m . **c** Sensor amplitude response, in terms of the change in contrast, ΔC , for different sensing times, T_{MW} . The signal frequency is tuned to $\omega_s = \omega_0 + \epsilon_m = (2\pi)2.557$ GHz. The dashed green line shows the maximum slope, $\max|\frac{\partial(\Delta C)}{\partial B}|$ for $T_{MW} = 300$ ns. **d** Minimum resolvable magnetic field, $\delta B_{min,\perp}$, as a function of measurement integration time.

used to characterise the sensor's response to out-of-plane fields, g_{\parallel} . We begin by positioning the wire adjacent to our device and for CCDD parameters of $\Omega = (2\pi)100$ MHz, $\epsilon_m = (2\pi)30$ MHz, $T_{MW} = 300$ ns, we measure the contrast as a function of signal frequency (Fig. 4a). Three resonances are observed; $\omega_s = \Omega - \epsilon_m \approx (2\pi)71$ MHz and $\omega_s = \Omega + \epsilon_m \approx (2\pi)129$ MHz are predicted for g_{\parallel} signal components in Eq. (8), whereas $\omega_s = \epsilon_m \approx (2\pi)29$ MHz originates from a resonance in a third rotating frame with respect to $\omega_m \sigma_z'$ (see Supplementary Note 3).

As with an in-plane signal, we are able to tune the frequency of these resonances with ϵ_m , and therefore determine a signal's frequency. In Fig. 4b, the contrast is plotted as a function of ϵ_m and ω_s , revealing the expected linear dependence of the resonances. For out-of-plane magnetic fields, the upper limit of the frequency range is limited by Ω , and therefore the available microwave power and the conversion efficiency of the CPW. The lower limit is currently determined by the CCDD protocol, which requires $\Omega > \epsilon_m$ and $\epsilon_m > \sim (2\pi)10$ MHz³⁶. This could be extended by concatenating a third drive term⁴⁷, by including quantum frequency mixing⁴⁸ or continuous heterodyne detection¹⁷. Figure 4c plots the amplitude response of the sensor, which again shows similarities to in-plane field sensing (Fig. 4c), where the monotonic range and sensitivity (slope) are dependent on the T_{MW} sensing time.

Magnetic field mapping

Finally, we provide a proof of principle demonstration of our hBN based sensor by mapping the magnetic field from the wire loop antenna. The sensor and readout laser spot are at fixed positions, whilst the antenna is positioned $\sim 50 \mu\text{m}$ above the sample and scanned in the XY-plane. For a resonant signal frequency, $\omega_s = \Omega - \epsilon_m = (2\pi)71$ MHz the magnetic field map is shown in Fig. 5a. Missing data in grey corresponds to positions where the

wire obscures the collection pathway. We compare this result to a Comsol simulation of the out-of-plane magnetic field, shown in Fig. 5b, and find good qualitative agreement. In particular, at the inner-side of the apex of the loop, the signal amplitude can be seen to reach a maximum then dip before reaching the wire, which is specific to the out-of-plane magnetic field component.

Away from the apex, the wire loop approximates two parallel wires, which allows us to demonstrate the sensors capacity to differentiate between the in plane and out of plane components of the magnetic field. With the X-position fixed, as indicated by the dashed line in Fig. 5a, the two parallel sections of wire are scanned along x , for signal frequencies $\omega_s = \Omega - \epsilon_m = (2\pi)71$ MHz and $\omega_s = \omega_0 + \epsilon_m = (2\pi)2.58$ GHz, corresponding to g_{\perp} and g_{\parallel} , respectively. The experimental results are shown in Fig. 5c, alongside a fit to the analytical solution of the Biot-Savart law for two parallel conductors (see Supplementary Note section 4). We find good agreement to the experiment for sensor to source distances of $87 \pm 2 \mu\text{m}$ and $73 \pm 2 \mu\text{m}$ for each section of parallel wire. Note, the magnetic field amplitude for g_{\perp} is small relative to g_{\parallel} . This is due to a reduced power output of the signal generator at higher frequencies, which is reflected in the current fit parameters $I_{\perp} = 16.2$ mA and $I_{\parallel} = 81.7$ mA. The close agreement between experiment and model shows the hBN sensors capability to map the spatial variation of high frequency magnetic fields, which is relevant for a host of applications, for example in imaging microwave circuitry and probing the near-field of antennas⁴⁹.

DISCUSSION

In this work, we have implemented a phase modulated CCDD sensing scheme with an ensemble of negatively charged boron vacancies in hBN, which is sensitive to both signal frequency and

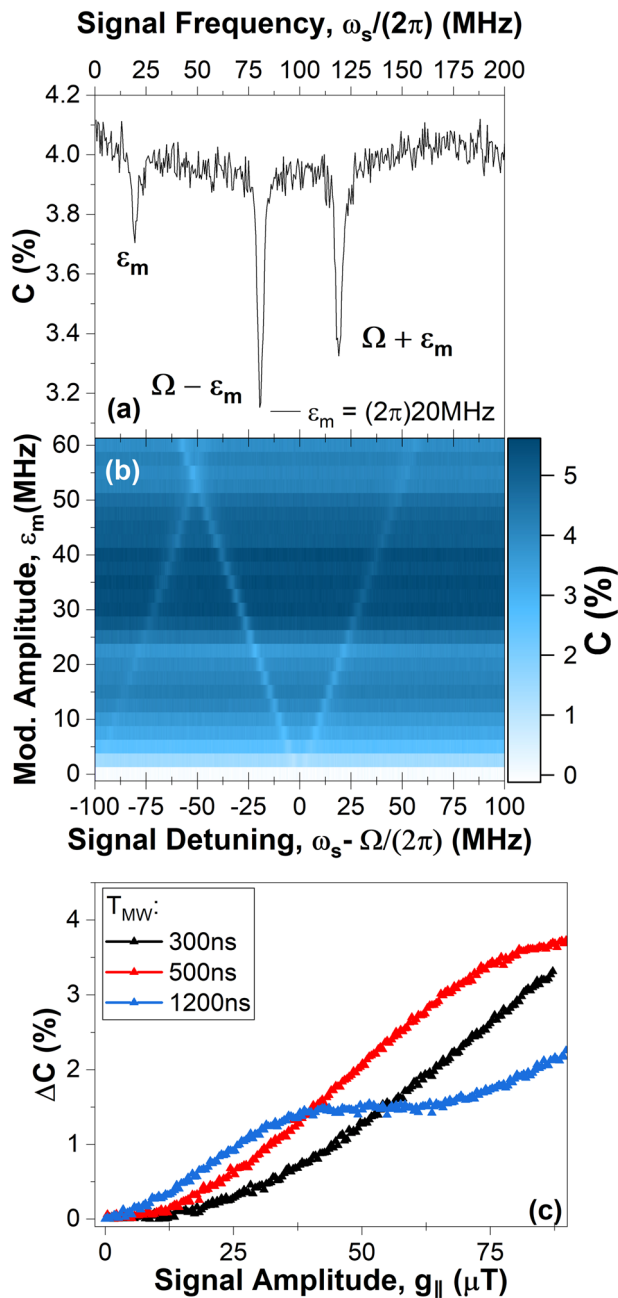


Fig. 4 Sensor response to out of plane AC magnetic field, $g_{||}$, from an external signal source. **a** Sensor frequency response for Rabi Frequency, $\Omega = (2\pi)100$ MHz and modulation amplitude, $\epsilon_m = (2\pi)20$ MHz, showing narrow bandwidth response at $g_{||}$ -specific frequencies $\omega_s = \pm \epsilon_m$ and $\omega_s = \Omega \pm \epsilon_m$. **b** Tuning of sensor frequency response with ϵ_m . **c** Sensor amplitude response for different T_{MW} when $\omega_s = \Omega - \epsilon_m$.

amplitude. The scheme avoids the timing errors associated with pulsed techniques, requires no phase matching of the signal field and benefits from sensitivities supported by coherence times approaching the T_1 limit, even at room temperature operation. In proof of principle experiments we have demonstrated a detectable frequency range of ± 150 MHz of the ESR for in plane fields and $\sim 10 - 150$ MHz for out of plane fields. We achieve a sensitivity of $\sim 1 \mu\text{T}/\sqrt{\text{Hz}}$ at ~ 2.5 GHz for in-plane fields, for an estimated sensor volume of only $\sim 0.1 \mu\text{m}^3$. The large Rabi-frequency, enabled by directly integrating the hBN layer with

the CPW, means that the sensor can be tuned over a range > 250 MHz for a fixed DC magnetic field.

In future work, the sensitivity could be enhanced by increasing the intensity of the read-out signal. For example, by improving the excitation and collection efficiencies, increasing the sensor volume and/or defect density, or by using brighter defect species^{50,51}. The spatial resolution of the mapping setup used for Fig. 5, which is currently limited to $\sim 0.5 \mu\text{m}$ by the diffraction limited laser spot size, could also be improved to ~ 10 nm with super resolution techniques⁵², or by using Fourier magnetic imaging⁵³.

Overall, this technique presents a competitive solution to the problem of sensing GHz magnetic fields, and with further development could utilise the two-dimensionality of the host material to dramatically enhance sensitivity, or even gain access to otherwise undetectable signals. This capability could open the door to sensing across diverse application areas, from utilising hBN's low cytotoxicity⁵⁴ to probe biomolecular dynamics^{55,56} to collective excitations in magnetic thin films for emerging computing architectures^{57,58}.

METHODS

Sample

The sample consists of a chromium/gold (5/170 nm thick) coplanar waveguide (CPW), with a $10 \mu\text{m}$ wide central conductor, on a sapphire substrate and designed to be matched to 50Ω at 4 GHz. An hBN flake, approximately 100 nm thick, is placed on top of the CPW using the PDMS transfer method. Boron vacancies are generated/activated using C ion irradiation with an energy of 10 keV and dose of $1 \times 10^{14} \text{ cm}^{-2}$. Further details can be found in Baber et al.³⁹.

Experimental setup

PL is excited using a 488 nm diode laser, modulated by an acousto-optic modulator. The laser is coupled to a long working distance objective lens (N.A.=0.8) which focuses the light to a diffraction-limited spot $\sim 0.5 \mu\text{m}$ in diameter. The wavelength is selected to be close to the maximum absorption efficiency³⁹. Photoluminescence is collected with the same objective, separated from the excitation laser with a dichroic beamsplitter and further filtered by a 750 nm long pass filter. A fibre-splitter couples the light to a pair of single photon avalanche diodes (SPAD), which effectively doubles the count rate before saturation. The PL intensity is recorded using a time-correlated single photon counting module (Swabian Time Tagger 20), which has a data transfer limit of 8.5 Mtags/s that ultimately limits the signal-to-noise ratio that is achieved. The microwave control waveforms are generated using an arbitrary waveform generator (Keysight M8195A) and amplifier (30 dB amplification, maximum output power 30 dBm) and are applied via a circulator to one end of the CPW. The signal source (Agilent 8648C) is connected to the other end of the CPW, via a second circulator. There is no clock synchronization between the control and signal sources. The optical and microwave excitation, APD gating and photon collection are synchronised using a digital pattern generator (Swabian Pulse Streamer). All measurements are performed with a DC magnetic field along the z-axis of ~ 40 mT generated by a permanent magnet.

The results presented are from two similar devices. Device A is used to collect the data in Figs. 2–4, with device B used to collect the magnetic field mapping data in Fig. 5. Due to a small difference in the sample heights relative to the permanent magnet, $\omega_0 = (2\pi)2.52$ GHz for device A and $\omega_0 = (2\pi)2.55$ GHz for device B.

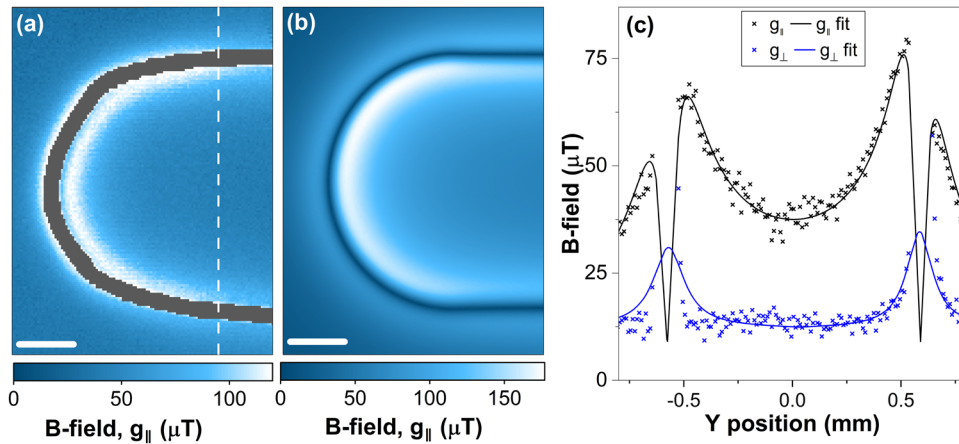


Fig. 5 Magnetic field mapping of a resonant AC signal. **a** Measured and **(b)** simulated XY-maps of the out of plane magnetic field component, $g_{||}$, from a $40\ \mu\text{m}$ diameter wire loop. The wire was driven with a signal frequency $\omega_s = \Omega - \epsilon_m = (2\pi)71\ \text{MHz}$ to meet the resonance condition of the CCD scheme. The sensor readout was integrated over 4 s for each $10\ \mu\text{m}^2$ pixel in **(a)**. The scale markers in **(a)** and **(b)** are $250\ \mu\text{m}$. Greyed-out areas correspond to sections where the wire obscures the photoluminescence collection path. **c** Scanning across the two parallel sections of wire described by the linecut in **(a)**, the in plane, g_{\perp} , and out of plane, $g_{||}$, magnetic field components of the signal are mapped using the g_{\perp} and $g_{||}$ -specific frequencies $\omega_s = \omega_0 + \epsilon_m = (2\pi)2580\ \text{MHz}$ and $\omega_s = \Omega - \epsilon_m = (2\pi)71\ \text{MHz}$, respectively. The solid lines show fits to the data using an analytical solution of the Biot-Savart law for two infinitely long parallel conductors (see Supplementary Note 4).

DATA AVAILABILITY

The datasets generated and/or analysed during the current study are available in the University of Exeter Repository repository, <https://doi.org/10.24378/exe.4905>.

CODE AVAILABILITY

The underlying code for this study is not publicly available but may be made available to qualified researchers on reasonable request from the corresponding author.

Received: 12 September 2023; Accepted: 5 December 2023;

Published online: 06 January 2024

REFERENCES

- Arai, K. et al. Millimetre-scale magnetocardiography of living rats with thoracotomy. *Commun. Phys.* **5**, 200 (2022).
- Hatano, Y. et al. High-precision robust monitoring of charge/discharge current over a wide dynamic range for electric vehicle batteries using diamond quantum sensors. *Sci. Rep.* **12**, 13991 (2022).
- Cao, Q.-Y. et al. Protecting quantum spin coherence of nanodiamonds in living cells. *Phys. Rev. Appl.* **13**, 24021 (2020).
- Shao, L., Zhang, M., Markham, M., Edmonds, A. M. & Lončar, M. Diamond radio receiver: Nitrogen-vacancy centers as fluorescent transducers of microwave signals. *Phys. Rev. Appl.* **6**, 064008 (2016).
- Schirhagl, R., Chang, K., Loretz, M. & Degen, C. L. Nitrogen-vacancy centers in diamond: Nanoscale sensors for physics and biology. *Annu. Rev. Phys. Chem.* **65**, 83–105 (2014).
- Rondin, L. et al. Magnetometry with nitrogen-vacancy defects in diamond. *Rep. Prog. Phys.* **77**, 056503 (2014).
- Balasubramanian, G. et al. Nanoscale imaging magnetometry with diamond spins under ambient conditions. *Nature* **455**, 648–651 (2008).
- Maze, J. R. et al. Nanoscale magnetic sensing with an individual electronic spin in diamond. *Nature* **455**, 644–647 (2008).
- Huxter, W. S., Sarott, M. F., Trassin, M. & Degen, C. L. Imaging ferroelectric domains with a single-spin scanning quantum sensor. *Nat. Phys.* **19**, 644–648 (2023).
- Gross, I. et al. Real-space imaging of non-collinear antiferromagnetic order with a single-spin magnetometer. *Nature* **549**, 252–256 (2017).
- Schirhagl, S. et al. Submillihertz magnetic spectroscopy performed with a nanoscale quantum sensor. *Science* **356**, 832–837 (2017).
- Boss, J. M., Cuijia, K. S., Zopes, J. & Degen, C. L. Quantum sensing with arbitrary frequency resolution. *Science* **356**, 837–840 (2017).
- Glenn, D. R. et al. High-resolution magnetic resonance spectroscopy using a solid-state spin sensor. *Nature* **555**, 351–354 (2018).
- Fescenko, I. et al. Diamond magnetometer enhanced by ferrite flux concentrators. *Phys. Rev. Res.* **2**, 023394 (2020).
- Wolf, T. et al. Subpicotesla diamond magnetometry. *Phys. Rev. X* **5**, 041001 (2015).
- Eisenach, E. R. et al. Cavity-enhanced microwave readout of a solid-state spin sensor. *Nat. Commun.* **12**, 1357 (2021).
- Wang, Z. et al. Picotesla magnetometry of microwave fields with diamond sensors. *Sci. Adv.* **8**, 8158 (2022).
- Alsid, S. T. et al. A solid-state microwave magnetometer with picotesla-level sensitivity. *Phys. Rev. Applied* **19**, 054095 (2023).
- Farfurnik, D., Jarmola, A., Budker, D. & Bar-Gill, N. Spin ensemble-based ac magnetometry using concatenated dynamical decoupling at low temperatures. *J. Opt.* **20**, 024008 (2018).
- Pham, L. M. et al. Enhanced solid-state multispin metrology using dynamical decoupling. *Phys. Rev. B* **86**, 45214 (2012).
- Ishikawa, T., Yoshizawa, A., Mawatari, Y., Watanabe, H. & Kashiwaya, S. Influence of dynamical decoupling sequences with finite-width pulses on quantum sensing for ac magnetometry. *Phys. Rev. Appl.* **10**, 54059 (2018).
- Loretz, M., Roskopf, T. & Degen, C. L. Radio-frequency magnetometry using a single electron spin. *Phys. Rev. Lett.* **110**, 017602 (2013).
- Kong, F. et al. Nanoscale zero-field electron spin resonance spectroscopy. *Nat. Commun.* **9**, 1563 (2018).
- Cohen, I., Aharon, N. & Retzker, A. Continuous dynamical decoupling utilizing time-dependent detuning. *Fortschritte der Phys.* **65**, 1600071 (2017).
- Wang, G., Liu, Y. X. & Cappellaro, P. Observation of the high-order mollow triplet by quantum mode control with concatenated continuous driving. *Phys. Rev. A* **103**, 022415 (2021).
- Farfurnik, D. et al. Experimental realization of time-dependent phase-modulated continuous dynamical decoupling. *Phys. Rev. A* **96**, 13850 (2017).
- Cai, J. M. et al. Robust dynamical decoupling with concatenated continuous driving. *New J. Phys.* **14**, 113023 (2012).
- Gottscholl, A. et al. Initialization and read-out of intrinsic spin defects in a van der waals crystal at room temperature. *Nat. Mater.* **19**, 540–545 (2020).
- Gottscholl, A. et al. Spin defects in hbn as promising temperature, pressure and magnetic field quantum sensors. *Nat. Commun.* **12**, 4480 (2021).
- Lyu, X. et al. Strain quantum sensing with spin defects in hexagonal boron nitride. *Nano Lett.* **22**, 6553–6559 (2022).
- Yang, T. et al. Spin defects in hexagonal boron nitride for strain sensing on nanopillar arrays. *Nanoscale* **14**, 5239–5244 (2022).
- Healey, A. J. et al. Quantum microscopy with van der waals heterostructures. *Nat. Phys.* **19**, 87–91 (2023).
- Huang, M. et al. Wide field imaging of van der waals ferromagnet fe₃gete₂ by spin defects in hexagonal boron nitride. *Nat. Commun.* **13**, 5369 (2022).
- Kumar, P. et al. Magnetic imaging with spin defects in hexagonal boron nitride. *Phys. Rev. Appl.* **18**, 061002 (2022).
- Rizzato, R. et al. Extending the coherence of spin defects in hBN enables advanced qubit control and quantum sensing. *Nat. Commun.* **14**, 5089 (2023).

36. Ramsay, A. J. et al. Coherence protection of spin qubits in hexagonal boron nitride. *Nat. Commun.* **14**, 461 (2023).
37. Haykal, A. et al. Decoherence of V_B^- spin defects in monoisotopic hexagonal boron nitride. *Nat. Commun.* **13**, 4347 (2022).
38. Gong, R. et al. Coherent dynamics of strongly interacting electronic spin defects in hexagonal boron nitride. *Nat. Commun.* **14**, 3299 (2023).
39. Baber, S. et al. Excited state spectroscopy of boron vacancy defects in hexagonal boron nitride using time-resolved optically detected magnetic resonance. *Nano Lett.* **22**, 461–467 (2022).
40. Stark, A. et al. Narrow-bandwidth sensing of high-frequency fields with continuous dynamical decoupling. *Nat. Commun.* **8**, 1105 (2017).
41. Wang, G., Liu, Y.-X. & Cappellaro, P. Coherence protection and decay mechanism in qubit ensembles under concatenated continuous driving. *New J. Phys.* **22**, 123045 (2020).
42. Degen, C. L., Reinhard, F. & Cappellaro, P. Quantum sensing. *Rev. Mod. Phys.* **89**, 035002 (2017).
43. Mathur, N. et al. Excited-state spin-resonance spectroscopy of V_B^- defect centers in hexagonal boron nitride. *Nat. Commun.* **13**, 3233 (2022).
44. Onizhuk, M. et al. Probing the coherence of solid-state qubits at avoided crossings. *PRX Quantum* **2**, 010311 (2021).
45. Zhou, F. et al. DC magnetic field sensitivity optimization of spin defects in hexagonal boron nitride. *Nano Lett.* **23**, 6209–6215 (2023).
46. Taylor, J. M. et al. High-sensitivity diamond magnetometer with nanoscale resolution. *Nat. Phys.* **4**, 810–816 (2008).
47. Cai, J.-M. et al. Robust dynamical decoupling with concatenated continuous driving. *New J. Phys.* **14**, 113023 (2012).
48. Wang, G. et al. Sensing of arbitrary-frequency fields using a quantum mixer. *Phys. Rev. X* **12**, 021061 (2022).
49. Horsley, A. et al. Microwave device characterization using a widefield diamond microscope. *Phys. Rev. Appl.* **10**, 44039 (2018).
50. Guo, N.-J. et al. Coherent control of an ultrabright single spin in hexagonal boron nitride at room temperature. *Nat. Commun.* **14**, 2893 (2023).
51. Stern, H. L. et al. Room-temperature optically detected magnetic resonance of single defects in hexagonal boron nitride. *Nat. Commun.* **13**, 618 (2022).
52. Khatri, P., Malein, R. N. E., Ramsay, A. J. & Luxmoore, I. J. Stimulated emission depletion microscopy with color centers in hexagonal boron nitride. *ACS Photonics* **8**, 2081–2087 (2021).
53. Arai, K. et al. Fourier magnetic imaging with nanoscale resolution and compressed sensing speed-up using electronic spins in diamond. *Nat. Nanotechnol.* **10**, 859–864 (2015).
54. Merlo, A., Mokkaapati, V. R. S. S., Pandit, S. & Mijakovic, I. Boron nitride nanomaterials: Biocompatibility and bio-applications. *Biomater. Sci.* **6**, 2298–2311 (2018).
55. Zhang, K., Ghosh, S., Saxena, S. & Dutt, M. V. G. Nanoscale spin detection of copper ions using double electron-electron resonance at room temperature. *Phys. Rev. B* **104**, 224412 (2021).
56. Shi, F. et al. Single-protein spin resonance spectroscopy under ambient conditions. *Science* **347**, 1135–1138 (2015).
57. Bertelli, I. et al. Magnetic resonance imaging of spin-wave transport and interference in a magnetic insulator. *Sci. Adv.* **6**, 3556–3567 (2020).
58. Prananto, D. et al. Probing thermal magnon current mediated by coherent magnon via nitrogen-vacancy centers in diamond. *Phys. Rev. Appl.* **10**, 64058 (2021).

ACKNOWLEDGEMENTS

This work was supported by the Engineering and Physical Sciences Research Council [Grant numbers EP/S001557/1 and EP/L015331/1], Partnership Resource Funding from the Quantum Computing and Simulation Hub [EP/T001062/1] and an Engineering and Physical Sciences Research Council iCASE in partnership with Oxford Instruments Plasma Technology. Ion implantation was performed by Keith Heasman and Julian Fletcher at the University of Surrey Ion Beam Centre. For the purpose of open access, the author has applied a 'Creative Commons Attribution (CC BY)' licence to any Author Accepted Manuscript version arising'.

AUTHOR CONTRIBUTIONS

I.J.L. and A.J.R. conceived and designed the experiments. S.B. fabricated the sample. I.J.L. and C.J.P. built the experimental setup and performed the measurements. I.J.L. and A.J.R. supervised the project. I.J.L., C.J.P., and A.J.R. analysed and discussed the experimental results. C.J.P., B.B.G., and A.J.R. performed calculations. C.J.P. wrote the manuscript with contributions from I.J.L. and A.J.R.

COMPETING INTERESTS

The authors declare no competing interests.

ADDITIONAL INFORMATION

Supplementary information The online version contains supplementary material available at <https://doi.org/10.1038/s41534-023-00796-4>.

Correspondence and requests for materials should be addressed to Charlie J. Patrickson.

Reprints and permission information is available at <http://www.nature.com/reprints>

Publisher's note Springer Nature remains neutral with regard to jurisdictional claims in published maps and institutional affiliations.



Open Access This article is licensed under a Creative Commons Attribution 4.0 International License, which permits use, sharing, adaptation, distribution and reproduction in any medium or format, as long as you give appropriate credit to the original author(s) and the source, provide a link to the Creative Commons license, and indicate if changes were made. The images or other third party material in this article are included in the article's Creative Commons license, unless indicated otherwise in a credit line to the material. If material is not included in the article's Creative Commons license and your intended use is not permitted by statutory regulation or exceeds the permitted use, you will need to obtain permission directly from the copyright holder. To view a copy of this license, visit <http://creativecommons.org/licenses/by/4.0/>.

© The Author(s) 2024